Revision 1: Synchrotron micro-spectroscopic examination of Indonesian nickel laterites

Rong Fan and Andrea R. Gerson*

Minerals and Materials Science & Technology, Mawson Institute, University of South Australia, Mawson Lakes, SA 5095, Australia

ABSTRACT

Nickel is typically distributed across a number of fine-grained minerals in nickel laterites, formed by intense tropical weathering of ultramafic rocks. Indonesia accounts for approximately 16% of the world's lateritic nickel reserves, which play an increasing role in global nickel production. However, relatively few geochemical studies of Indonesian laterites have been undertaken and quantification of Ni speciation is unclear. In this study the Ni geochemistry of an Indonesian laterite composed of limonite and saprolite has been examined using synchrotron microprobe analysis (microprobe X-ray fluorescence microscopy, μ-XFM; microprobe X-ray diffraction, μ-XRD; microprobe X-ray absorption spectroscopy; μ-XAS) and bulk XAS. This approach provides semi-quantitative species specific information not readily obtainable using traditional laboratory methods which are hampered by the fine grained heterogeneous nature of laterites. In the limonite 16 ± 4 % of the Ni was found to be substituted for Al in lithiophorite with 26 ± 7 % being associated with lizardite (a serpentine) substituted for Mg. A minor

* Corresponding author. Fax: +61 8 83025545
Email address: Andrea.Gerson@unisa.edu.au (A.R. Gerson)

proportion of the Ni is adsorbed onto the Mn layers of phyllomanganate (*e.g.* lithiophorite). However the majority of the Ni, 58 ± 15 % is substituted for Fe in goethite. The majority of the Ni (85 ± 21 %) within the saprolite is found to be associated with lizardite, the predominant mineral. A few relatively large Ni asbolane grains are also observed which account for 14 ± 3 % of the Ni with the remaining 1 ± 0.3 % of the Ni replacing Fe within goethite.

Keywords: Indonesian nickel laterite, limonite and saprolite, X-ray absorption spectroscopy, synchrotron microprobe, μ-XRD, μ-XFM

INTRODUCTION

Nickel laterites are formed by intense tropical weathering of ultramafic rocks, such as peridotites and serpentinites (Golightly 1981). The resulting profiles can be highly variable due to factors such as climate, topography, drainage and other hydrological influences, mineralogy and bedrock structure (Gleeson et al. 2003). Despite the diversity of lateritic profiles, some common features can be found enabling laterite types to be classified as oxide, clay or silicate laterites (Brand et al. 1998).

On prolonged weathering ultramafic strata decompose releasing mobile elements such as Fe, Ni, Mg and Si. Fe and Al are less soluble than Mg and Si and hence are enriched in the upper zone forming the oxide limonite layer which is rich in goethite, hematite and Mn oxides. Ni and Co are also strongly incorporated and co-precipitated into Mn oxides such as lithiophorite and asbolane (Elias 2001). Some Ni percolates from the overlying limonite layer and is incorporated into the underlying hydrous silicate saprolite layer which is rich in serpentine minerals (Elias

2001). Silicate laterites are formed after a long period of aggressive weathering. The saprolite zone may also occasionally be composed of clay minerals, predominantly the smectite clay nontronite. Clay laterites are formed in less severe weathering conditions (Gaudin et al. 2005).

Ni speciation within a wide variety of mineral samples, such as goethite (de Carvalho-e-Silva et al. 2003; Manceau et al. 2000; Singh et al. 2002), phyllomanganate (Manceau et al. 1987; Manceau et al. 2002b; Peacock and Sherman 2007; Peña et al. 2010; Roqué-Rosell et al. 2010) and phyllosilicates (Dähn et al. 2006; Kiczka et al. 2010; Manceau and Calas 1985; Manceau and Calas 1986) has been extensively investigated. However, these studies have mostly focused on individual mineral rather than natural laterites where Ni is typically distributed across a number of fine-grained minerals.

Traditional mineralogical measurements of such fine grained and heterogeneous samples, such as powder X-ray diffraction and selective chemical extraction, provide bulk, volume-averaged data that obscure important spatially variable information. Bulk XAS also provides volume-averaged information regarding the local environments of the metal of interest. The interpretation of bulk XAS data for a material containing multiple species, as is frequently the case in an ore or soil sample, requires a complete database of reference spectra. Microprobe XAS probes individual grains at a micron scale, offering selective local information that can be utilised in the interpretation of bulk XAS data. Synchrotron-based μ-XFM (microprobe X-ray fluorescence microscopy), μ-XRD (microprobe X-ray diffraction) and μ-XAS (microprobe X-ray absorption spectroscopy), together with bulk XAS analysis, provide a powerful tool to examine both lateritic samples at micron scale and also semi-quantitative analysis of the predominant Ni associations within the bulk materials.

Indonesia accounts for approximately 16 % of the world's lateritic nickel reserves, which play an increasing role in global nickel production (Berger et al. 2011). As for Philippine's laterites, and due to the similar climatic conditions, Indonesian nickel laterites generally contain only upper oxide and lower silicate zones, *e.g*. limonite and saprolite respectively (Dalvi et al. 2004). However, relatively few geochemical studies of Indonesian laterites have been undertaken and quantification of Ni speciation is unclear.

Synchrotron-based XAS methods have recently been applied in nickel laterites of Philippine (Fan and Gerson 2011) and New Caledonia (Dublet et al. 2012), providing comprehensive details of Ni speciation in these two types of nickel laterites. The study presented here focuses on the speciation and distribution of Ni within the complex fine grained mineral assemblage present in an Indonesian limonite and saprolite laterite indicating a significantly different profile of Ni distributions compared to those in Philippine and New Caledonia.

MATERIALS AND METHODS

Samples and reference materials

The ore samples were obtained from Raja Ampat, West Papua, Indonesia (Fan and Gerson 2013). The limonite ore was selected from the upper Fe-rich laterite fraction (2 – 3 m) and the saprolite ore from the lower Mg-rich laterite fraction (5 – 6 m). Both ore samples collected (≈20 kg each) were dried and homogenised, and 1 kg representative sample for each ore was crushed and ground to obtain fine grains. The paste pH of the ore samples was measured in suspensions with a solid/liquid weight ratio of 1:2, after 10 min shaking and overnight settling. The pH values are 5.5 and 7.7 for limonite and saprolite ores, respectively. Particle size analysis

(Matersizer 2000) suggests the iron-rich limonite ore contained around 80 % of particles less than 30 μm in size. In contrast, the particle size of the saprolite ore is not as fine with 40 % of the saprolite particles being less than 30 μm in size, and around 35 % of the saprolite particles being larger than 100 μm. Large rocks of diameter greater than 5 cm are also found in the saprolite ore.

The ores were embedded in resin, mounted onto a silicon backing plate (0.5 mm thick, Sigma Aldrich) and then polished to a thickness of ≈40 μm for synchrotron microprobe measurements. For bulk XAS, the ores were ground by hand with an agate mortar and pestle.

A synthetic goethite sample containing 1.9 mol% Ni, referred to hereafter as Goet, was used as a XAS reference. Its synthesis and characterisation are detailed elsewhere (Fan and Gerson 2011). Lizardite sample was obtained commercially from GEO Discoveries Australia Co. The phase purity of these materials was confirmed by bulk XRD. EXAFS spectra of asbolane and lithiophorite (referred to hereafter as Asb and Lith) were provided by Alain Manceau (ISTerre, CNRS and Université Joseph Fourier) with description and characterisation of these two standards being provided in Manceau et al. (1987) and Manceau et al. (2002), respectively. An EXAFS spectrum of Ni-sorbed birnessite, referred to hereafter as NiBi, was provided by Caroline Peacock (University of Leeds). The synthesis methodology and characterisation of the resultant solid are provided in Peacock and Sherman (2007).

Analytical methods

Mineralogical analysis.

The samples were dry ground to a fine powder in an agate mortar and pestle for elemental composition analysis. Metal concentrations in the solids were determined using inductively coupled plasma-atomic emission spectrometry (ICP-AES, Table 1).

Lab-based mineralogical studies of the ore samples were performed and are described in (Fan and Gerson 2013). Rietveld analysis of the XRD data indicated that the limonite ore is composed of 78 ± 5 wt% goethite, 2 ± 1 wt% lizardite (serpentine group mineral), 1 ± 1 wt% maghemite (spinel), 2 ± 1 wt% gibbsite, 3 ± 1 wt% quartz, 6 ± 2 wt% clinopyroxene, 6 ± 2 wt% talc, 1 ± 1 wt% hercynite (spinel), 0.5 ± 0.8 wt% enstatite and a small component of (approx, 1 wt%) unidentified material. It is estimated that the limonite ore contains approximately 5 wt% phyllomanganate based on the assumption that all the 1.6 wt% Mn is associated within phyllomanganate. This assumption is supported by SEM analyse which did not show Mn to be present in detectable concentrations in goethite grains selected from the limonite ore (Fan and Gerson 2013).

For the saprolite ore, Rietveld XRD analysis indicated that it contains 27 ± 3 wt% lizardite, 21 ± 3 wt% goethite, 10 ± 2 wt% enstatite, 3 ± 1 wt% diopside, 5 ± 2 wt% olivine, and 5 ± 2 wt% montmorillonite.

Synchrotron microprobe analysis.

Bulk Ni K-edge XAS spectra of the ores and synthetic Ni containing goethite were collected in fluorescence mode at the Australian National Beamline Facility (ANBF), Beamline 20B (bend magnet) at the Photon Factory synchrotron (2.5 GeV) KEK, Tsukuba, Japan. A water-cooled Si(111) channel cut double crystal monochromator was used to select the incident beam energy and the incident beam size was 2 × 1 mm in the horizontal and vertical directions,

130 respectively. A Canberra 36 element Ge-detector was positioned at 90° to the incident beam for
131 fluorescence XAS measurement. The energy was calibrated simultaneously to the XAS
132 measurement using a Ni foil positioned after the sample stage between the second and the third
133 ion chambers (Foran et al. 2007). The first ion chamber is located before the sample stage and is
134 used to record the incident beam intensity. The energy grid used was: 20 eV over the pre-edge
135 region from 8120 to 8320 eV; 2 eV over the edge region from 8320 to 8380 eV followed by *k*
136 increments of 0.05 until *k* equalled 13. Dwell time per step was 2 s. Various numbers of scans
137 (from 4 to 7) were recorded depending on the signal-to-noise ratio. Deadtime corrections were
138 not necessary as the intensity of the photon flux received by the detector was adjusted to insure a
139 linear response (typically total counts per detector per second less than 10,000 at deadtime above
140 0.7 ns) either by moving the detector away from the sample or placing Al foils between the
141 sample and detector to attenuate the signal arising from concentrated samples.

142 μ-XFM, μ-XRD and μ-XAS measurements were conducted at beamline 10.3.2 of the
143 Advanced Light Source (ALS), Lawrence Berkeley National Laboratory, Berkeley, USA
144 (Marcus et al. 2004). The beamline is equipped with a fixed exit Si(111) double-crystal
145 monochromator and a Kirkpatrick-Baez mirror pair to focus the beam to a spot size adjustable
146 from 5 × 5 μm to 16 × 7 μm. The chemical associations of Mn, Fe, Ni, Cr, Co, Zn and Cu in the
147 laterite samples were imaged by scanning the sample stage using incident beam energy of 17
148 keV. The step count time for fine scans was 200 ms, and the beam dimension was adjusted to be
149 5 × 5 μm while the step size was 5 μm. Characteristic elemental fluorescence emission intensities
150 were measured with a Canberra seven-element Ge solid-state detector mounted at 90° to the
151 incident beam and were normalised relative to the intensity of the incident beam.

X-ray fluorescence spectra of each 'hotspot' chosen from the μ-XFM maps was collected for 240 s with excitation energy of 17 keV, enabling, in principle, the detection of the K-lines of all the elements of interest. The spectra were quantified using PyMCA software (Solé et al. 2007).

μ-XRD was performed on selected representative regions of interest using incident beam energy of 17 keV with a Bruker SMART6000 CCD detector in transmission geometry. Exposure times ranged from 60 s to 360 s. Diffraction parameters, such as sample-to-detector distance, wavelength, and detector orientation parameters, *etc.*, were calibrated using corundum. XRD profiles were extracted from the CCD image using the Fit2d software (Hammersley 1999). Background removal and subsequent phase identification were performed using DiffracPlus EVA software (Bruker) with the ICDD-PDF2 database (International Center for Diffraction Data 2000).

Multiple μ-XAS spectra were collected in fluorescence mode using the same seven-element Ge detector as for μ-XFM measurements. The energy grid for the Ni K XAS scan employed 5 eV increments over the pre-edge region from 8231 to 8311 eV; 0.5 eV increments over the edge region from 8311 to 8361 eV followed by a *k* increment 0.04 until a *k* of 13 was reached. The dwell time was set to 2 s for the pre-edge region, 3 s for the edge region and 3 to 8 s for the post-edge region.

To obtain spectra of adequate quality for both bulk and μ-XAS, it was necessary to average multiple datasets for each sample. EXAFS data reduction was carried out using the software packages ATHENA and ARTEMIS (Ravel and Newville 2005). For EXAFS data analysis the *k* range was fixed at 2.5 to 11, the *r* range was fixed at 1 to 3.5 and the *kw* weighting was fixed at 3. The amplitude reduction factor *S02* was fixed at 1 and the accuracy of this value

was verified by EXAFS fitting of the synthetic goethite samples. Linear least-squares combination fitting (LCF) analyses in *k* space for the bulk limonite and saprolite were performed to provide quantitative Ni compositions using ATHENA. LCF identified components should be considered accurate to ± 25% of their stated values (Kim et al. 2000; Ostergren et al. 1999).

RESULTS AND DISCUSSION

Limonite μ-XFM

Figure 1 shows a synchrotron μ-XFM elemental distribution map of Ni, Mn and Fe of the limonite ore. It is clear that Fe is dominant over the region with some Fe-rich particles being up to 100 μm in size which are likely to be agglomerates of fine-grained goethite particles. The red and green coloured particles (Ni-rich and Mn-rich, respectively) are also highly variable in size, being up to approximately 50 μm.

The spatial distributions of Ni demonstrate significant fine-scale heterogeneity which is consistent with previous SEM/EDS observations (Fan and Gerson 2013). Ni association with Mn can be seen as yellow coloured regions within the limonite ore μ-XFM map (Figure 1a) and this association is further demonstrated by the strong statistical correlation in the scatter plot shown in Figure 1b. Each spot in the scatter plot represents a pixel in the μ-XFM map and the *x* and *y* coordinates are Mn and Ni counts, respectively. The Pearson function, ρ, has been applied to assess the correlations quantitatively (Manceau et al. 2002a). A ρ value of 1 indicates a perfect positive correlation whereas -1 demonstrates a perfect negative correlation. The ρ value of the scatter plot in Figure 1b is equal to 0.81 indicating significant correlation of Ni with Mn. However, there is also a significant amount of Ni that is not associated with Mn as demonstrated by the vertical grouping of spots next to the *y*-axis of Figure 1b. In this case, the ρ function

198 approach can be misleading because clearly Ni and Mn are from a small fraction of the sample
199 and are present in a few isolated grains. Hence the rest of the sample is devoid of one of the two
200 elements (Manceau et al. 2002a). Two Ni-Mn hotspots were chosen for further analyses (Spot 1
201 and 2, Figure 1a).

202 Significant Ni is also found associated with non-Mn containing grains (such as Spots 3 -
203 6, Figure 1). Ni is found to be also associated with Fe, which is demonstrated in the scatter plot
204 (Figure 2c) indicating a smaller degree of correlation of Ni and Fe than with Mn, with ρ value of
205 0.21. This may suggest that a significant amount of the Ni is not associated with Fe rich grains.
206 Spots 5 and 6 were chosen for Ni-Fe association examination while Spots 3 and 4 show no
207 significant Ni-Mn or Ni-Fe associations.
208
209 **Saprolite μ-XFM**
210 The synchrotron XRF map of the saprolite ore is provided in Figure 2a. As for the
211 limonite ore, the Ni within the saprolite ore is distributed heterogeneously. Again, the yellow
212 coloured regions represent Ni-Mn association while the purple regions demonstrate Ni-Fe
213 association. The Pearson function, ρ, for the Ni-Mn correlation map (Figure 2b) is equal to 0.51,
214 which is significantly smaller than the 0.84 for the Ni-Mn correlation map (Figure 1b) for the
215 limonite ore. This smaller correlation is likely to be due to the small fraction of phyllomangante
216 in the saprolite ore, suggested by the smaller concentration of Mn in the saprolite (0.1 wt%)
217 compared to that in the limonite (1.6 wt%). Some large Fe-rich particles were found by μ-XFM
218 of the saprolite. In contrast to the Fe (42.3 wt%) and Ni concentrations (1.2 wt%) in the limonite,
219 there is smaller concentration of Fe in the saprolite (10.4 wt%) and relatively greater Ni
220 concentration (2.6 wt%). This suggests that a significant amount of the Ni in the saprolite is

probably not associated with Fe. A relatively high ρ value (0.61) for the Ni-Fe correlation map (Figure 2c) is still observed, probably due to the ubiquitous distribution of Fe oxyhydroxides. Four Ni-containing locations (Spot 1 for Ni-Mn association, Spots 2 and 3 for non Ni-Mn or Ni-Fe associations, Spot 4 for Ni-Fe association) were selected for μ-XRD and μ-XAS analyses (Figure 2a).

Synchrotron microprobe characterisation of Ni-containing minerals

Phyllomanganate.

Figure 3 presents the μ-XRD patterns of the three Ni-Mn spots chosen from the μ-XRF maps of the limonite and saprolite ores. Spots 1 and 2 of the limonite show similar diffraction peaks at the *d*-spacings of 9.40, 4.70, 2.36, 1.88, 1.45 and 1.38 Å (Figure 3), which are similar to *d*-spacings of lithiophorite ($(Al,Li)(MnO_2)_2(OH)_2 \cdot nH_2O$, PDF card number 41-1378). The first two *d*-spacings, 9.40 and 4.70 Å, correspond to the 003 and 006 reflections. The lithiophorite structure consists of a stack of sheets of MnO_6 octahedra alternating with sheets of $(Li,Al)(OH)_6$ octahedra and transition metals such as Ni and Co commonly substitute into the structure (Ostwald 1984). The stronger intensities and narrower widths of the diffraction peaks for Spot 2 suggest lithiophorite in Spot 2 may have a greater degree of crystallinity compared to that at Spot 1 but differences in peak intensities may also be due to factors such as variations in texture and number of diffracting crystallites. XRD phase identification at limonite Spots 1 and 2 indicates that goethite is present as well as lithiophorite (Figure 3).

Asbolane, another important phyllomanganate mineral, has a similar crystal structure as lithiophorite but the Li-Al layers are replaced by Ni-Co layers (Manceau et al. 1987). At saprolite Spot 1, diffraction peaks occur at *d*-spacings 9.54 4.77, 2.40, 1.71 and 1.41 Å, which is

similar to the *d*-spacings of asbolane of 9.6, 4.8, 2.4 and 1.4 Å (Chukhrov et al. 1982). Asbolane may contain irregular mixed-layer stacking of Li-Al and Ni-Co layers and consequently displays variable composition and a range of XRD features (Becquer et al. 2006; Ostwald 1984).

μ-XANES of the limonite and saprolite Ni-Mn spots are presented in Figure 4a as compared to those of phyllomanganate references (NiBi, Lith and Asb). Data of the goethite standard is also shown. Comparison of the data from the Ni-Mn spots (limonite Spot 1 and 2, saprolite Spot 1) indicates a considerable degree of similarity to those of NiBi, Lith and Asb but dissimilarity to the data from goethite. Although both phyllomanganate and goethite are observed by μ-XRD for limonite Spot 1 and 2 it appears more likely that Ni is associated with phyllomanganate.

EXAFS fitting has been conducted for the locations of limonite Spot 1 and 2 (Table 2 and Figure 5). The peaks of the Fourier transform of the normalised background subtracted EXAFS data from Spot 1 (Figure 1a) have similar positions and amplitude to those arising from ^{TC}Ni complexes (Manceau et al. 2007). This has also been observed for a phyllomanganate within a Philippine limonite (Fan and Gerson 2011). The least-squares fit of the data confirms this and indicates that 6.2(2.5) Mn atoms are present at the Ni to Mn distance of 3.49(5) Å (Table 2 and Figure 5), suggesting that the Ni in limonite Spot 1 is probably absorbed on the Mn octahedral layer rather than substituting for Mn within the Mn layer which gives rise to a Ni-Mn distance of typically 2.91 Å (Manceau et al. 2002b).

For limonite Spot 2, both Ni K-edge XANES and EXAFS spectra (Figure 5) are almost identical to that of Lith (lithiophorite reference where Ni replaces Al, Manceau et al. (2002b)). Both spectra have a unique peak split at *k* of 4 Å^{-1} (pointed to by the arrow in Figure 5a), which has not been observed in any other Ni phyllomanganate spectra. Further analysis reveals that the

Ni-O and Ni-Al distances are equal to 2.04(1) and 2.97(3) Å, respectively, which is similar to the values of Ni substituting for Al in lithiophorite found previously (Manceau et al. 1987; Manceau et al. 2002b).

Analysis of the μ-XRD patterns indicates asbolane (phyllomanganate) is present within saprolite Spot 1. Comparison of the XANES of these hotspots (Figure 4a) suggests a clear similarity between saprolite Spot 1 and asbolane, implying that the Ni at saprolite Spot 1 is associated with asbolane. It is difficult for EXAFS to distinguish between elements of nearly the same atomic number, such as Ni and Co. However, in this case only a Ni-Ni distance is considered for the second shell as previous studies have suggested that Co in asbolane is within the layers of either $(Mn,Co)(OH)_2$ or possibly CoOOH or $Co(OH)_3$ (Manceau et al. 1987; Manceau et al. 1992). EXAFS analysis suggests Ni is surrounded by 6 O at 2.05(1) Å and 1.9(8) Ni at 3.07(4) Å (Table 2). Ni K-edge EXAFS spectra of asbolane and lithiophorite are clearly distinct. Furthermore, the Ni-Al distance in lithiophorite has been found to be equal to 2.94 Å whereas Ni-Ni the distance in asbolane equal to 3.03 Å (Manceau et al. 1986; Manceau et al. 2002b). The Ni-Ni distance derived of 3.07(4) Å also implies that the Ni is more likely to be present in the $Ni(OH)_2$ layers in asbolane than substituted for Al in lithiophorite.

Lizardite.

Ni is also found at some locations (limonite Spots 3 and 4, saprolite Spots 2 and 3), where Mn is not found and Fe concentrations are small compared to Fe rich particles, such as limonite Spot 5 and saprolite Spot 4. μ-XRD analyses of these spots indicate that serpentine (lizardite) is present at all of them (Figure 6). As for phyllomanganate, differences in intensities

and widths of μ-XRD peaks cannot be directly related to crystallites as there are other factors such as texture that may also contribute. XRF spectra suggest that Ni within these spots (data not shown) is less concentrated than in the Mn enriched grains, such as limonite Spot 1, but considerably more concentrated than that in goethite (*e.g.* limonite Spot 5).

The XANES profiles (Figure 4) for limonite Spots 3 and 4, saprolite Spots 2 and 3 and lizardite, are very similar (Manceau and Calas 1985; Manceau and Calas 1986). A shoulder just below the absorption edge (Figure 4a) is observed for all these spots as well as lizardite. This is due to a small distortion of the octahedral environment, indicating the existence of Ni phyllosilicate.

EXAFS analysis for Spots 3 and 4 of the limonite ore and Spots 2 and 3 of the saprolite ore (Figure 7) using the structure of lizardite 1T as a starting model reveals Ni has a similar local structure to the Mg site, which implies Ni replaces Mg in the lizardite structure. The fitted parameters for all these spots are provided in Table 3. The Ni-O distance is equal to 2.06(1) Å for all the spots. The Ni-Ni distances ranges from 3.06(4) to 3.10(4) Å while the Ni-Si distances are 3.23(4) to 3.33(4) Å for the first and second cationic shells respectively, which are consistent with known Ni-lizardite structural parameters (Manceau 1990). The same structure was also found for the Philippine saprolite ore (Fan and Gerson 2011).

Goethite.

μ-XRD analyses (Figure 8) suggest that goethite is the predominant mineral present in the Fe enriched grains (limonite Spots 5 and 6, saprolite Spot 4). μ-XRF spectra for limonite Spot 5 suggested the presence of Ni in association with Fe.

311 It is difficult to measure Ni EXAFS for these Fe containing grains due to the strong Fe
312 fluorescence occurring at the Ni K-edge and a large number of scans were needed to obtain
313 reasonable data. Figure 9 provides a comparison of the experimental and fitted Ni K-edge
314 EXAFS and Fourier transforms for limonite Spot 5 and goethite.

315 EXAFS analysis of the synthetic Ni containing goethite reveals a Ni-O distance of 2.04(1)
316 Å and three Ni-Fe distances of 3.03(3), 3.31(4) and 3.52(4) Å (Table 4, Figure 9). The three Ni-
317 Fe shells corresponds to the edge-sharing linkage along the *c* direction, the edge-sharing linkage
318 along the *b* direction and the double-corner linkage along the *a* direction, respectively. In the
319 goethite crystal structure, the three respective Fe-Fe distances are 3.01, 3.28 and 3.50 Å
320 (Sampson 1969). Our results (3.08(3), 3.32(4) and 3.53(4) Å for limonite Spot 5 and 3.03(3),
321 3.31(4) and 3.52(4) Å for the synthetic goethite, Table 4, Figure 9) are slightly longer than the
322 Fe-Fe distances in goethite, probably due to the larger ionic radius of Ni^{2+} (0.69 Å) as compared
323 to Fe^{3+} (0.65 Å) (Shannon and Prewitt 1969). The second Ni-Fe distance has been reported
324 previously to be 3.18 Å (Manceau et al. 2000) and 3.21 Å (de Carvalho-e-Silva et al. 2003). Both
325 of which are significantly smaller than our Ni-Fe values (3.32(4) Å for limonite Spot 5 and
326 3.31(4) Å for the synthetic goethite) and the Fe-Fe value from goethite crystal structure (3.28 Å).
327 The authors attribute this reduced distance to the contraction of octahedra in the *bc* plane and
328 expansion in the *ab* plane. It has also been demonstrated previously in many studies that Ni is
329 present within the goethite lattice rather than being surface adsorbed (Dublet et al. 2012;
330 Georgiou and Papangelakis 1998). Our results also confirm the Ni is in the form of Fe
331 replacement within goethite structure.
332
333

334 **Bulk EXAFS analysis**

335 A comparison of the XANES and EXAFS data arising from the bulk limonite and
336 saprolite, standards and spots is shown in Figure 4. There is clear similarity of the XANES data
337 between the bulk limonite and goethite, which is confirmed by LCF analysis. LCF of the EXAFS
338 spectra (in *k*-space) of goethite, lithiophorite (Ni replaces Al), birnessite, and lizardite was
339 utilised to fit the spectra of the limonite bulk sample. Ni association with birnessite in the form of
340 the TC configuration is observed from μ-XAS, but the fraction of this form is small as is
341 apparent from inspection of the Fourier transform data in Figure 4 and is also confirmed by LCF
342 (Figure10a and b). The best fit is obtained using three spectra (goethite, lizardite and
343 lithiophorite) which suggests that 58 ± 15 % of the Ni in the limonite replaces Fe within goethite;
344 26 ± 7 % of the Ni in the bulk limonite is associated with lizardite as replacement of Mg and the
345 remaining Ni is associated with lithiophorite where Ni replaces Al.

346 There is a clear similarity of the XANES and EXAFS data among the bulk saprolite,
347 lizardite and lizardite-containing hotspots in both the limonite and saprolite (Figure 4), implying
348 that the Ni association with lizardite is dominant in the saprolite ore. LCF of the bulk Ni EXAFS
349 (Figure 10c and d) of the saprolite suggest that 85 ± 21 % Ni in the saprolite replaces Mg in
350 lizardite, only about 14 ± 3 % of the Ni is within the $Ni(OH)_2$ layer within asbolane and only 1 ±
351 0.3 % of the Ni is associated with goethite through replacement of Fe. Ni in saprolite is mainly
352 associated with lizardite which has been quantitatively confirmed by previous studies (Dublet et
353 al. 2012; Fan and Gerson 2011). This is also observed by SEM examinations of an Indonesian
354 saprolite containing 2 wt% Ni suggest a diverse Ni distribution with Ni mainly being associated

355 with Mg silicate and Mg-Fe silicate (mainly serpentine, olivine, chlorite and amphibole) and in
356 smaller concentrations with goehite, Mn oxide and magnetite (Chen et al. 2004).
357
358 ## IMPLICATIONS
359
360 ### Comparison to other nickel laterites
361 The dominance of Ni in goethite (58 ± 15 % Ni) within the limonite ore examined here is
362 significantly different in comparison to a Philippine limonite examined previously where 60 ±
363 15 % of the Ni was found to be associated with phyllomanganate, with the remaining 40 ± 10 %
364 incorporated into goethite through replacement of the Fe (Fan and Gerson 2011). However, there
365 is similarity to a New Caledonian laterite from 34 m depth where 65 % of the Ni was found to be
366 present in goethite with 21 % in phyllomanganate and 14 % in lizardite (Dublet et al. 2012). This
367 New Caledonian sample represents a transition zone from saprolite to limonite, which is marked
368 by a sharp increase of Fe to 47.8 wt% and a sharp decrease of Si to 3.2 wt%. This is very similar
369 to the Fe and Si contents, 42.3 wt% and 3.4 wt% respectively, in the Indonesian limonite. The
370 New Caledonian transition laterite was found to be mainly composed of forsterite, enstatite and
371 serpentine. The Ni-containing serpentine mineral lizardite is found in both the Indonesian and the
372 New Caledonian limonites. Moreover, there is significant Ni concentration within the Indonesian
373 limonite lizardite (26 ± 7 % Ni) considering the low concentration of lizardite (2 ± 1 wt%) in the
374 ore. In contrast for the Philippine limonite mineralogical analyses by XRD and SEM suggested
375 the absence of serpentine minerals (Fan and Gerson 2011). The similarity of the New Caledonian
376 transition laterite and Indonesian limonite in terms of Ni speciation and concentrations of major

377 elements suggests that they may result from similar weathering processes of ultramafic rock.
378 The paste pH values of the Indonesian limonite and saprolite were found to be pH 5.5 (2
379 – 3 m depth) and pH 7.7 (5 – 6 m depth), respectively, compared to pH 6.3 for the Philippine
380 limonite (7 – 9 m depth) and pH 7.3 for the Philippine saprolite (21 – 23 m depth). The pH
381 profile of the New Caledonian lateritic samples was found to vary from pH 9 in the bedrock to
382 pH 6 in the upper-most sample (Fandeur et al. 2009). More acidic conditions are found in the
383 upper limonite horizon due to humic acids generated by decay of organic material (Geophysics
384 Research Board, 1981). The geochemical conditions (*e.g.* pH) and hydrogeological conditions
385 (*e.g.* permeability) may have a significant impact on Ni speciation and distributions within the
386 lateritic profile. It has been reported that Ni tends to absorb above the Mn octahedral layer within
387 phyllomanganate at low pH, whereas substitution of Ni for Mn in Mn layer occurs on pH
388 increase (Manceau et al. 2007; Peacock and Sherman, 2007). The bulk and μ-EXAFS studies
389 described here suggest that Ni is adsorbed onto the Mn layers of phyllomanganate in the acidic
390 limonite, implying pH may be a controlling parameter for Ni association and formation of the
391 phyllomanganate.
392 The concentration of Ni in serpentines (85 ± 21 %) for the Indonesian saprolite examined
393 here is greater than any of the New Caledonian saprolites (Dublet et al. 2012) where typically
394 less than 70 % of the Ni was found to be associated with serpentine with the remaining Ni being
395 located within goethite. However, it is similar to that of the Philippine saprolite ore where 90 %
396 of the Ni is associated with serpentine with the remaining located within phyllomanganate (Fan
397 and Gerson 2011). The sampling depths are apparently different: 5 – 6 m for Indonesian saprolite,
398 21 – 23 m for the Philippine saprolite and a variety of depths below 37 m for the New

399 Caledonian saprolites. Ni association within phyllomanganate was not found in most of the New
400 Caledonian saprolites with the exception of the 52.5 m sample where Ni phyllomanganate
401 accounts for 13 %. The presence of Ni phyllomanganate in both the Philippine and Indonesian
402 saprolites may be related to the relatively shallower sampling depth. It has been suggested that
403 Ni-containing phyllomanganate occurs as generally veins and coatings particularly at the lowest
404 part of the upper limonite horizon (Dalvi et al. 2004).
405

406 **Implications for hydrometallurgy of nickel laterites**

407 Improved knowledge of the forms of Ni present in nickel laterites is essential for better
408 understanding of industrial leaching mechanism and thus the design of cost-effective nickel
409 concentration and leaching strategies. A reducing reagent, e.g. sulfur dioxide, may be used to
410 adjust redox potential for the dissolution of phyllomanganates (Vanbrabant et al. 2013) but is not
411 required for the dissolution of other major Ni-containing minerals, e.g. goethite and lizardite.
412 The application of reducing reagents may not be economic if Ni concentration in
413 phyllomanganates is not significant. For instance, 60 ± 15 % of the Ni is associated with
414 phyllomanganates in the Philippine limonite (Fan and Gerson 2011), compared to 16 ± 4 % in
415 the Indonesian limonite. It may therefore be essential to use reducing reagents for
416 hydrometallurgical process of the Philippine limonite in order to dissolve phyllomanganates and
417 release most of the Ni. This demonstrates that a good understanding of the mineralogy of an ore,
418 particularly full definition of multiple sources of valuable metals, is important in mineral
419 processing with optimum extractive efficiency.
420

ACKNOWLEDGEMENTS

This research has been supported by the Premier's Science and Research Fund of South Australia and co-sponsored by BHP-Billiton and Rio Tinto. We would like to thank Michael Cheah and Garry Foran for their assistance during our bulk EXAFS measurements at the ANBF at the Photon Factory. We are grateful to Matthew Marcus and Sirine Fakra for aid with the synchrotron microprobe measurements at the Advanced Light Source, end-station 10.3.2. The authors also thank Alain Manceau and Caroline Peak for their generous provision of EXAFS spectra of phyllomanganate references.

We are grateful to the ALS and ANBF for the instrument time allocations. The use of the ALS at Lawrence Berkeley National Laboratory is supported by the Director, Office of Science, Office of Basic Energy Sciences, Materials Sciences Division, of the U.S. Department of Energy under Contract No. DE-AC03-76SF00098. The work performed at the Australian National Beamline Facility was supported by the Australian Synchrotron Research Program, which is funded by the Commonwealth of Australia under the Major National Research Facilities Program.

The authors also thank the Access to Major Research Facilities Program (AMRFP) for the provision of the travel funds for overseas synchrotron visits. Rong Fan acknowledges support from University of South Australia for award of postgraduate UniSA President's Scholarship.

REFERENCES

Becquer, T., Quantin, C., Rotte-Capet, S., Ghanbaja, J., Mustin, C., and Herbillon, A.J. (2006) Sources of trace metals in ferralsols in New Caledonia. European Journal of Soil Science, 57, 200-213.

444 Berger, V.I., Singer, D.A., Bliss, J.D., and Moring, B.C. (2011) Ni-Co laterite deposits of the
445 world; database and grade and tonnage models. U.S. Geological Survey Open-File Report
446 2011-1058.
447 Brand, N.W., Butt, C.R.M., and Elias, M. (1998) Nickel laterites: classification and features.
448 AGSO Journal of Australian Geology and Geophysics, 17, 81-88.
449 Chen, T.T., Dutrizac, J.E., Krause, E., and Osborne, R. (2004) Mineralogical characterization of
450 nickel laterites from New Caledonia and Indonesia. International Laterite Nickel
451 Symposium, Proceedings of [a] Symposium held during the TMS Annual Meeting,
452 Charlotte, NC, United States, Mar. 14-18, 2004, 79-99.
453 Chukhrov, F.V., Gorshkov, A.I., Vitovskaya, I.V., Drits, V.A., and Sivtsov, A.V. (1982) On the
454 nature of cobalt-nickel asbolane; a component of some supergene ores. Special
455 Publication of the Society for Geology Applied to Mineral Deposits, 2, 230-9.
456 Dähn, R., Jullien, M., Scheidegger, A.M., Poinssot, C., Baeyens, B., and Bradbury, M.H. (2006)
457 Identification of neoformed Ni-phyllosilicates upon Ni uptake in montmorillonite: a
458 transmission electron microscopy and extended x-ray absorption fine structure study.
459 Clays and Clay Minerals, 54, 209-219.
460 Dalvi, A.D., Bacon, W.G., and Osborne, R.C. (2004) The Past and the Future of Nickel Laterites.
461 PDAC 2004 International Convention, Trade Show & Investors Exchange, p. 1-27.
462 de Carvalho-e-Silva, M.L., Ramos, A.Y., Tolentino, H.C.N., Enzweiler, J., Netto, S.M., and
463 Alves, M.d.C.M. (2003) Incorporation of Ni into natural goethite: An investigation by X-
464 ray absorption spectroscopy. American Mineralogist, 88, 876-882.

Dublet, G., Juillot, F., Morin, G., Fritsch, E., Fandeur, D., Ona-Nguema, G., and Brown Jr, G.E. (2012) Ni speciation in a New Caledonian lateritic regolith: A quantitative X-ray absorption spectroscopy investigation. Geochimica et Cosmochimica Acta, 95, 119-133.

Elias, M. (2001) Nickel laterite deposits – geological overview, resources and exploitation. In D.R. Cooke, and J. Pongratz, Eds. Giant Ore Deposits: Characteristics, genesis and exploration, 4, p. 205-220. CODES Special Publication, Centre for Ore Deposit Research, University of Tasmania.

Fan, R., and Gerson, A.R. (2011) Nickel geochemistry of a Philippine laterite examined by bulk and microprobe synchrotron analyses. Geochimica et Cosmochimica Acta, 75, 6400-6415.

Fan, R., and Gerson, A.R. (2013) Mineralogical characterisation of Indonesian laterites prior to and post atmospheric leaching. Hydrometallurgy, 134–135, 102-109.

Fandeur, D., Juillot, F., Morin, G., Olivi, L., Cognigni, A., Ambrosi, J.-P., Guyot, F., and Fritsch, E. (2009) Synchrotron-based speciation of chromium in an Oxisol from New Caledonia: Importance of secondary Fe-oxyhydroxides. American Mineralogist, 94, 710-719.

Foran, G., Hester, J., Garrett, R., Dressler, P., Fonne, C., Beau, J.-O., and Lampert, M.-O. (2007) New 36-element Pixel Array Detector at the ANBF - choosing the right detector for your Beamline. AIP Conference Proceedings, 882, p. 881-883.

Gaudin, A., Decarreau, A., Noack, Y., and Grauby, O. (2005) Clay mineralogy of the nickel laterite ore developed from serpentinized peridotites at Murrin Murrin, Western Australia. Australian Journal of Earth Sciences, 52, 231-241.

Geophysics Research Board (1981) Mineral Resources: Genetic Understanding for Practical Applications, National Academy Press, Washington, D.C. Georgiou, D., and

Papangelakis, V.G. (1998) Sulfuric acid pressure leaching of a limonitic laterite: chemistry and kinetics. Hydrometallurgy, 49, 23-46.

Gleeson, S.A., Butt, C.R.M., and Elias, M. (2003) Nickel laterites: a review. SEG Newsletter, 54, 11-18.

Golightly, J.P. (1981) Nickeliferous laterite deposits. Economic Geology, 75, 710-735.

Golightly, J.P., and Arancibia, O.N. (1979) The chemical composition and infrared spectrum of nickel- and iron-substituted serpentine from a nickeliferous laterite profile, Soroako, Indonesia. Canadian Mineralogist, 17, 719-728.

Hammersley, A. (1999) FIT2D, version 10.31. Tech. Rep. ESRF, Grenoble, France.

International Center for Diffraction Data (2000). Newtown Square, PA, USA.

Kiczka, M., Wiederhold, J.G., Frommer, J., Kraemer, S.M., Bourdon, B., and Kretzschmar, R. (2010) Iron isotope fractionation during proton- and ligand-promoted dissolution of primary phyllosilicates. Geochimica et Cosmochimica Acta, 74, 3112-3128.

Kim, C.S., Brown, G.E., and Rytuba, J.J. (2000) Characterization and speciation of mercury-bearing mine wastes using X-ray absorption spectroscopy. The Science of The Total Environment, 261, 157-168.

Manceau, A. (1990) Distribution of cations among the octahedra of phyllosilicates: Insight from EXAFS. Canadian Mineralogist, 28, 321-8.

Manceau, A., and Calas, G. (1985) Heterogeneous distribution of nickel in hydrous silicates from New Caledonia ore deposits. American Mineralogist, 70, 549-58.

Manceau, A., and Calas, G. (1986) Nickel-bearing clay minerals: II. Intracrystalline distribution of nickel: An x-ray absorption study. Clay Minerals, 21, 341-60.

509 Manceau, A., Gorshkov, A.I., and Drits, V.A. (1992) Structural chemistry of manganese, iron,
510 cobalt, and nickel in manganese hydrous oxides: Part II. Information from EXAFS
511 spectroscopy and electron and x-ray diffraction. American Mineralogist, 77, 1144-57.
512 Manceau, A., Lanson, M., and Geoffroy, N. (2007) Natural speciation of Ni, Zn, Ba, and As in
513 ferromanganese coatings on quartz using x-ray fluorescence, absorption, and diffraction.
514 Geochimica et Cosmochimica Acta, 71, 95-128.
515 Manceau, A., Llorca, S., and Calas, G. (1986) Structural chemistry of manganese, cobalt, and
516 nickel in some natural manganese oxides. Journal de Physique, Colloque, 2, 703-707.
517 Manceau, A., Llorca, S., and Calas, G. (1987) Crystal chemistry of cobalt and nickel in
518 lithiophorite and asbolane from New Caledonia. Geochimica et Cosmochimica Acta, 51,
519 105-113.
520 Manceau, A., Marcus, M.A., and Tamura, N. (2002a) Quantitative speciation of heavy metals in
521 soils and sediments by synchrotron X-ray techniques. Reviews in Mineralogy and
522 Geochemistry, 49, 341-428.
523 Manceau, A., Schlegel, M.L., Musso, M., Sole, V.A., Gauthier, C., Petit, P.E., and Trolard, F.
524 (2000) Crystal chemistry of trace elements in natural and synthetic goethite. Geochimica
525 et Cosmochimica Acta, 64, 3643-3661.
526 Manceau, A., Tamura, N., Marcus, M.A., MacDowell, A.A., Celestre, R.S., Sublett, R.E.,
527 Sposito, G., and Padmore, H.A. (2002b) Deciphering Ni sequestration in soil
528 ferromanganese nodules by combining X-ray fluorescence, absorption, and diffraction at
529 micrometer scales of resolution. American Mineralogist, 87, 1494-1499.

Marcus, M.A., MacDowell, A.A., Celestre, R., Manceau, A., Miller, T., Padmore, H.A., and Sublett, R.E. (2004) Beamline 10.3.2 at ALS: a hard X-ray microprobe for environmental and materials sciences. Journal of Synchrotron Radiation, 11, 239-247.

Ostergren, J.D., Brown, G.E., and Tingle, T.N. (1999) Quantitative speciation of lead in selected mine tailings from Leadville, CO. Enviromental Science & Technology, 33, 1627-1636.

Ostwald, J. (1984) Two varieties of lithiophorite in some Australian deposits. Mineralogical Magazine, 48, 383-388.

Peacock, C.L., and Sherman, D.M. (2007) Crystal-chemistry of Ni in marine ferromanganese crusts and nodules. American Mineralogist, 92, 1087-1092.

Peña, J., Kwon, K.D., Refson, K., Bargar, J.R., and Sposito, G. (2010) Mechanisms of nickel sorption by a bacteriogenic birnessite. Geochimica et Cosmochimica Acta, 74, 3076-3089.

Purwanto, H., Shimada, T., Takahashi, R., and Yagi, J.-i. (2003) Recovery of Nickel from Selectively Reduced Laterite Ore by Sulphuric Acid Leaching. ISIJ International, 43, 181-186.

Ravel, B., and Newville, M. (2005) ATHENA, ARTEMIS, HEPHAESTUS: data analysis for x-ray absorption spectroscopy using IFEFFIT. Journal of Synchrotron Radiation, 12, 537-541.

Roqué-Rosell, J., Mosselmans, J.F.W., Proenza, J.A., Labrador, M., Gal, S., Atkinson, K.D., and Quinn, P.D. (2010) Sorption of Ni by "lithiophorite-asbolane" intermediates in Moa Bay lateritic deposits, eastern Cuba. Chemical Geology, 275, 9-18.

Sampson, C.F. (1969) Lattice parameters of natural single crystal and synthetically produced goethite (α-FeOOH). Acta Crystallographica Section B: Structural Science, 25, 1683-5.

552 Shannon, R.D., and Prewitt, C.T. (1969) Effective ionic radii in oxides and fluorides. Acta
553 Crystallographica Section B: Structural Science, 25, 925-946.
554 Singh, B., Sherman, D.M., Gilkes, R.J., Wells, M.A., and Mosselmans, J.F.W. (2002)
555 Incorporation of Cr, Mn and Ni into goethite (α-FeOOH): mechanism from extended X-
556 ray absorption fine structure spectroscopy. Clay Minerals, 37, 639-649.
557 Solé, V.A., Papillon, E., Cotte, M., Walter, P., and Susini, J. (2007) A multiplatform code for the
558 analysis of energy-dispersive X-ray fluorescence spectra. Spectrochimica Acta Part B:
559 Atomic Spectroscopy, 62, 63-68.
560 Vanbrabant, Y., Burlet, C., and Louis, P. (2013) Mineralogical Characterization of Cobaltic
561 Oxides from the Democratic Republic of Congo. In T. Battle, M. Moats, V. Cocalia, H.
562 Oosterhof, S. Alam, A. Allanore, R. Jones, N. Stubina, C. Anderson, and S. Wang, Eds.
563 Ni–Co 2013, p. 241-254. John Wiley & Sons, Inc.
564
565
566
567

568 **Table 1** Elemental composition of the limonite and saprolite (wt%).

Sample	Al	Co	Cr	Fe	Mg	Mn	Ni	S	Si
Limonite	5.4	0.3	1.0	42.3	0.2	1.6	1.2	0.3	3.4
Saprolite	1.1	0.0	0.2	10.4	14.0	0.1	2.6	0.0	19.0

569

570

571 **Table 2** Structural parameters *R* (Å), *CN* and σ (Å) derived from the EXAFS data analysis of
572 three phyllomanganate-containing hotspots.

Location	Bond	*R*	*CN*	σ	ΔE	*Res*
limonite Spot 1	Ni-O	2.07(1)	6[a]	0.006(1)	-3.7	24
	Ni-Mn	3.49(5)	6.2(2.5)	0.020(4)		
limonite Spot 2	Ni-O	2.04(1)	6[a]	0.006(1)	-4.6	21
	Ni-Al	2.97(3)	2.2(9)	0.005(1)		
saprolite Spot 1	Ni-O	2.05(1)	6[a]	0.007(1)	-1.9	26
	Ni-Ni	3.07(4)	1.9(8)	0.007(1)		

573 *R* - interatomic distance; *CN* - coordination number; σ - Debye-Waller factor; ΔE -inner potential
574 correction in eV; *Res* - reduced χ^2; interval of the inverse Fourier transform: 1.0–3.5 Å; [a] Fixed
575 value.

576

577

578

579 **Table 3** Structural parameters *R* (Å), *CN* and σ (Å) derived from the EXAFS data analysis of

580 lizardite.

Location	Bond	*R*	*CN*	Σ	ΔE	*Res*
limonite Spot 3	Ni-O	2.06(1)	6[a]	0.007(1)	-4.1	8.0
	Ni-Ni	3.10(4)	2.8(1.1)	0.006(1)		
	Ni-Si	3.26(4)	3.8(1.5)	0.013(3)		
limonite Spot 4	Ni-O	2.06(1)	6[a]	0.007(1)	-2.8	10.6
	Ni-Ni	3.06(4)	3.3(1.3)	0.004(1)		
	Ni-Si	3.33(4)	3.3(1.3)	0.003(1)		
saprolite Spot 2	Ni-O	2.06(1)	6[a]	0.006(1)	-3.3	6.0
	Ni-Ni	3.09(4)	5.2(2.1)	0.010(2)		
	Ni-Si	3.25(4)	2.9(1.1)	0.003(1)		
saprolite Spot 3	Ni-O	2.06(1)	6[a]	0.008(1)	-3.9	7.3
	Ni-Ni	3.08(4)	7.2(2.9)	0.010(2)		
	Ni-Si	3.23(4)	3.4(1.4)	0.008(2)		

581 *R* - interatomic distance; *CN* - coordination number; σ - Debye-Waller factor; ΔE -inner potential

582 correction in eV; *Res* - reduced χ^2; interval of the inverse Fourier transform: 1.0–3.5 Å**;** [a] Fixed value.

583

584 **Table 4** Structural parameters *R* (Å), *CN* and σ (Å) derived from the EXAFS data analysis of
585 synthetic Ni goethite and limonite Spot 5.

Location	Bond	*R*	*CN*	Σ	ΔE	*Res*
Goethite	Ni-O	2.04(1)	6[a]	0.005(1)	-5.0	24.1
	Ni-Fe	3.03(3)	2.7(1.1)	0.010(3)		
	Ni-Fe	3.31(4)	1.9(8)	0.010(3)[b]		
	Ni-Fe	3.52(4)	3.3(1.3)	0.010(3)[b]		
limonite Spot 5	Ni-O	2.04(1)	6[a]	0.006(1)	-5.3	4.0
	Ni-Fe	3.08(3)	1.4(8)	0.005(1)		
	Ni-Fe	3.32(4)	2.1(9)	0.005(1)[c]		
	Ni-Fe	3.53(4)	2.5(1.2)	0.005(1)[c]		

586 *R* - interatomic distance; *CN* - coordination number; σ - Debye-Waller factor; ΔE -inner potential
587 correction in eV; *Res* - reduced χ^2; interval of the inverse Fourier transform: 1.0–3.5 Å**;** [a] Fixed value; [b,c]
588 Fixed to the value determined for Ni-Fe.
589

590

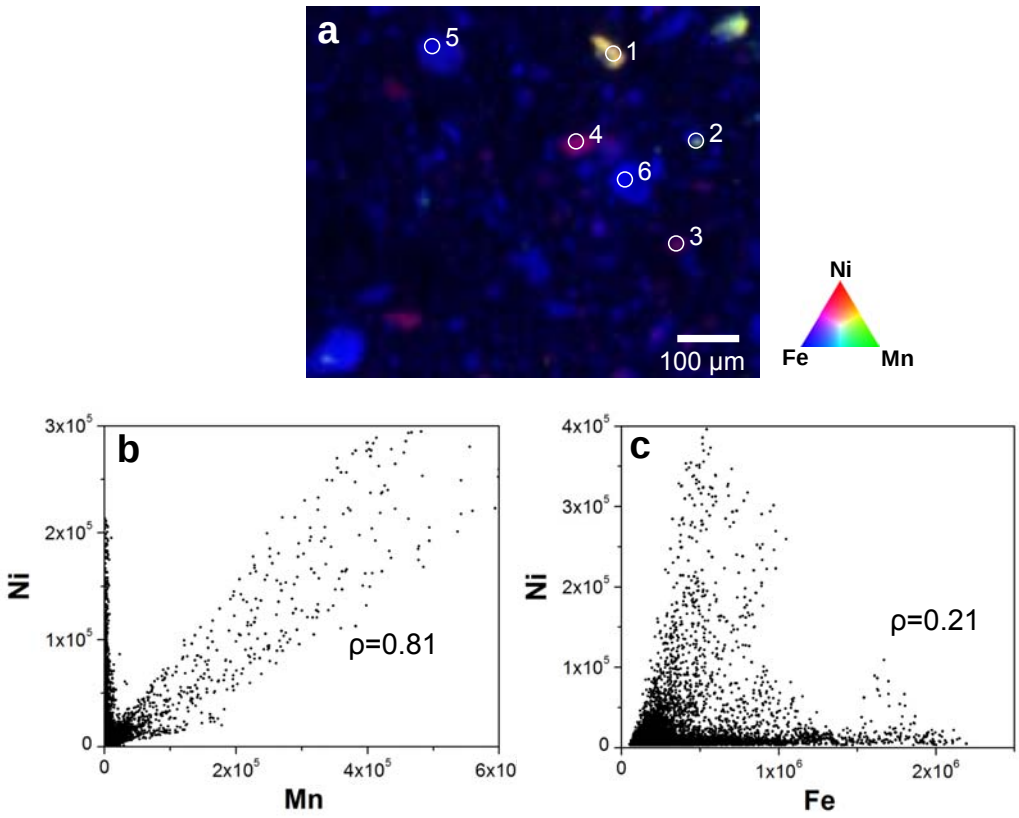

591

592 **Figure 1.** (a) 600 × 750 µm synchrotron µ-XFM map of a selected region of the
593 limonite sample. This tri-coloured map shows the elemental distributions of Ni (red), Mn
594 (green) and Fe (blue). Two scatter plots for Ni-Mn correlation (b), and Ni-Fe correlation (c),
595 are given for the same region. Six locations on (a) (Spots 1 - 6) were chosen for further µ-
596 XRF, µ-XRD and µ-XAS analyses. Spot 1 and 2 are rich in both Mn and Ni. Spot 3 and 4 are
597 rich in Ni only while Spot 5 and 6 are rich in Ni and Fe.

598

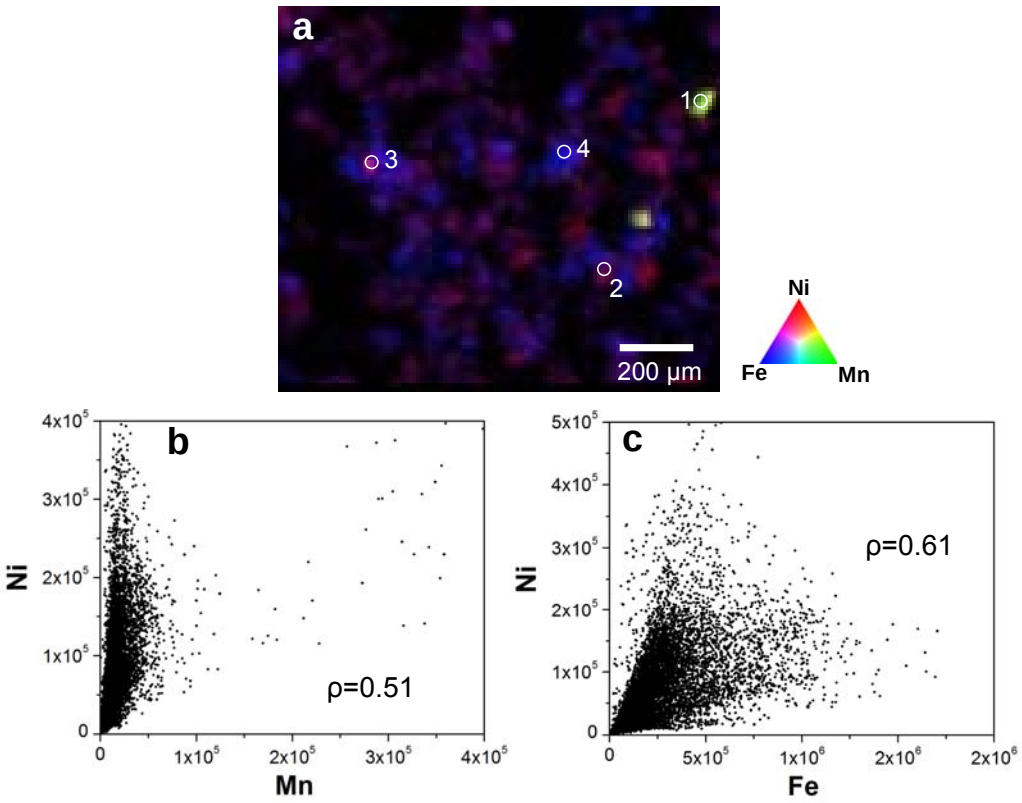

Figure 2. 1200 × 1000 μm synchrotron μ-XFM map of a selected region of the saprolite sample (a), and scatter plots for the Ni-Mn correlation (b), and the Ni-Fe correlation (c), for the same region.

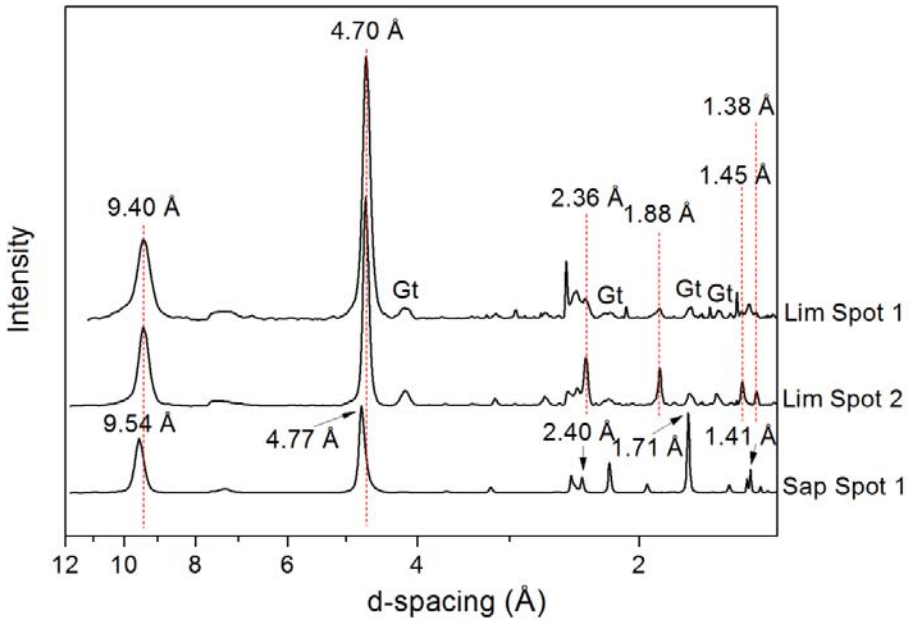

604

605 **Figure 3.** μ-XRD patterns collected at the X-ray energy of 17 keV for two locations
606 selected from the limonite μ-XFM map (limonite Spot 1 and 2, see Figure 1a) and one
607 location selected from the saprolite μ-XFM map (saprolite Spot 1, see Figure 2a).

608

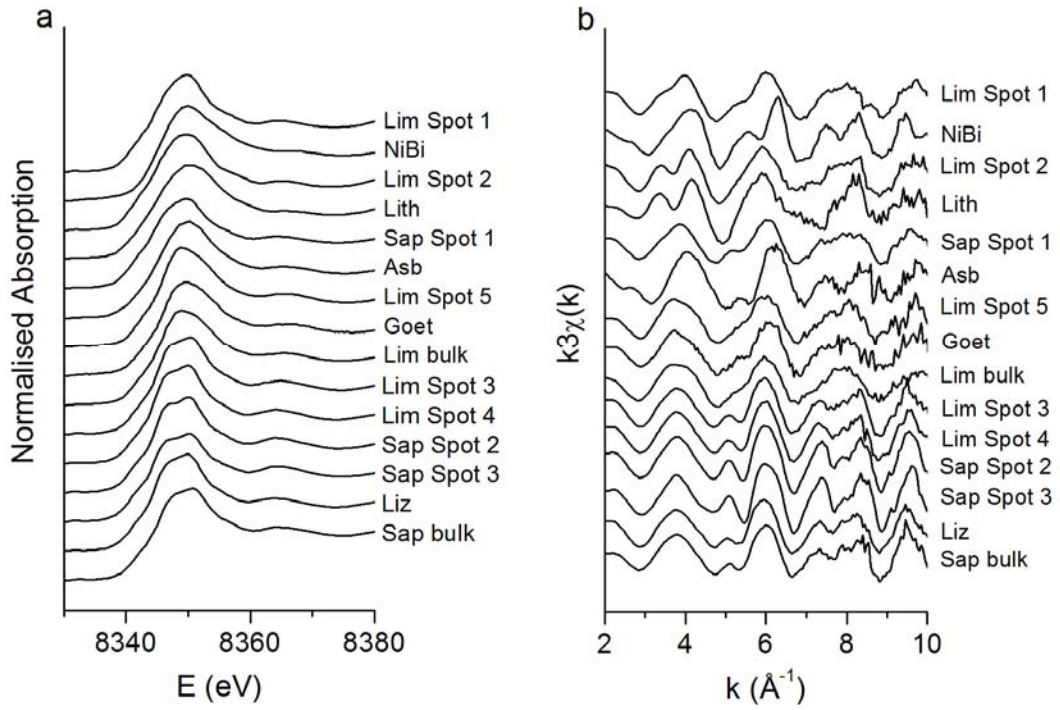

609

610 **Figure 4.** Comparison of normalised XANES (a), and EXAFS (b), at the Ni K-edge
611 of selected locations from the μ-XFM map of limonite and saprolite (limonite Spots 1 – 5
612 from Figure 1a, saprolite Spots 1 – 3 from Figure 2a), bulk limonite and saprolite samples
613 and the spectra of a series of references, Goet (Ni goethite), NiBi (birnessite), Liz (Ni
614 lizardite), Lith (lithiophorite, Ni replaces Al) and Asb (asbolane).

615

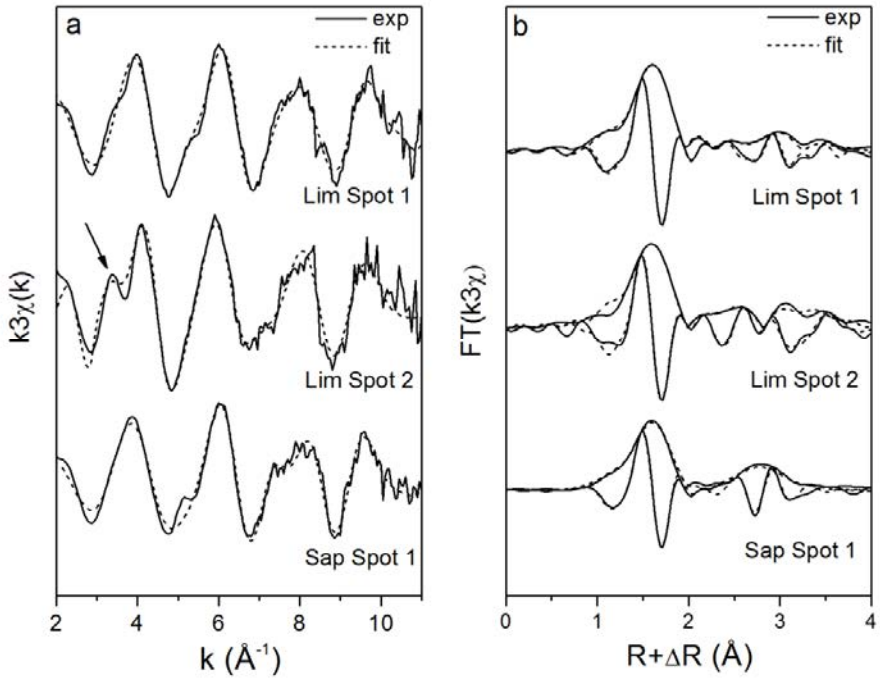

616

617 **Figure 5.** Experimental and fitted Ni K-edge EXAFS spectra (a), and magnitude and

618 imaginary part of their Fourier transforms (b), for limonite Spots 1 and 2 and saprolite Spot 1.

619

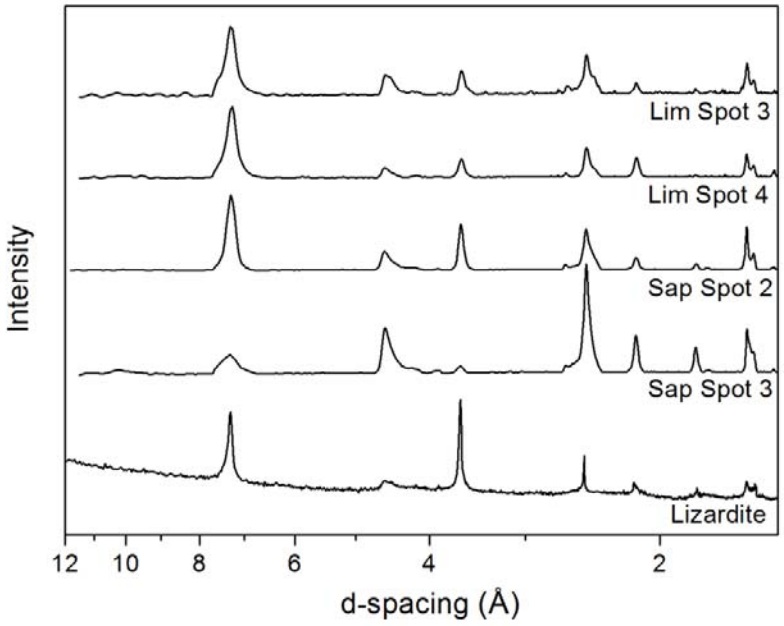

620

621 **Figure 6.** μ-XRD patterns collected at X-ray energy of 17 keV for two locations
622 selected from the limonite μ-XFM map (Spots 3 and 4, Figure 1a) and two locations selected
623 from the saprolite μ-XFM map (Spots 2 and 3, Figure2a). Bulk XRD of lizardite collected
624 using Co Kα radiation is also presented to compare with the μ-XRD results.

625

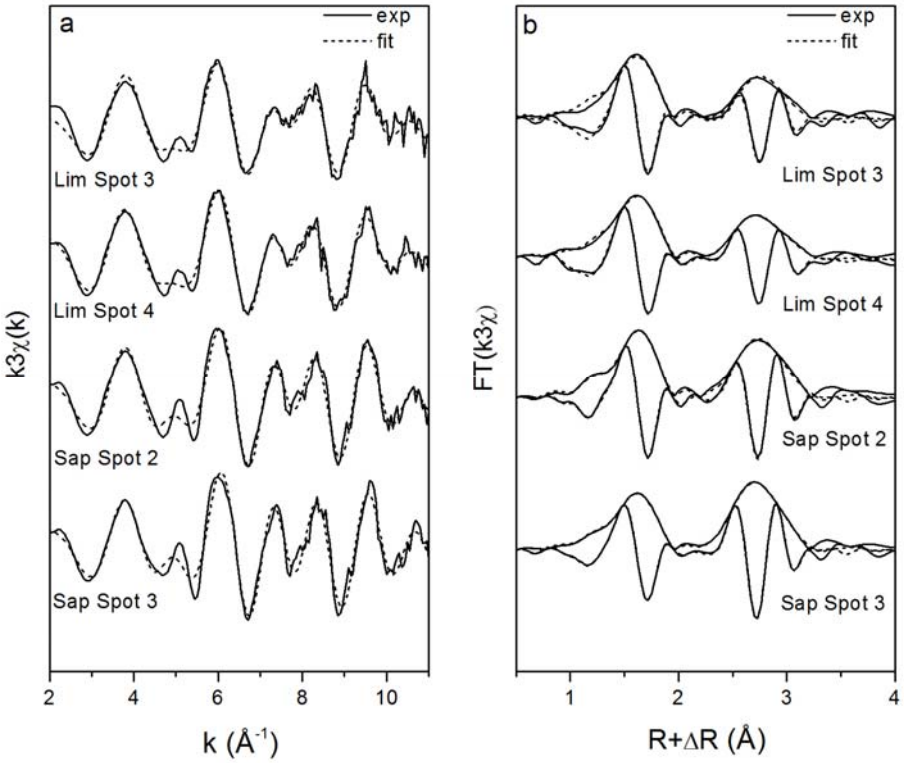

Figure 7. Experimental and fitted Ni K-edge EXAFS spectra (a), and magnitude and imaginary part of their Fourier transforms (b), for limonite Spots 3 and 4 and saprolite Spots 2 and 3.

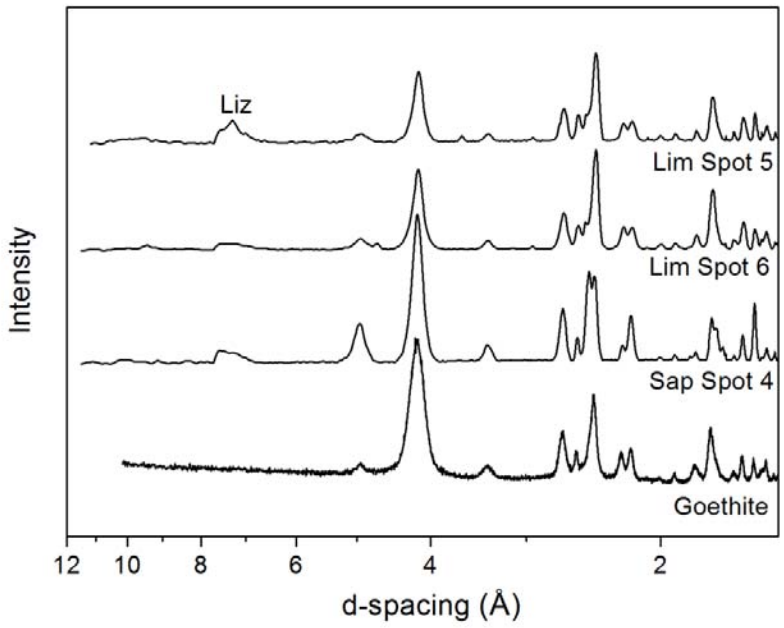

631

632 **Figure 8.** μ-XRD patterns collected at X-ray energy of 17 keV for two locations
633 selected from the limonite μ-XFM map (limonite Spots 5 and 6, Figure 1a) and one location
634 selected from the saprolite μ-XFM map (saprolite Spot 4, Figure 2a). Bulk XRD of synthetic
635 goethite collected using Co Kα radiation is also presented to compare with the μ-XRD
636 results.

637

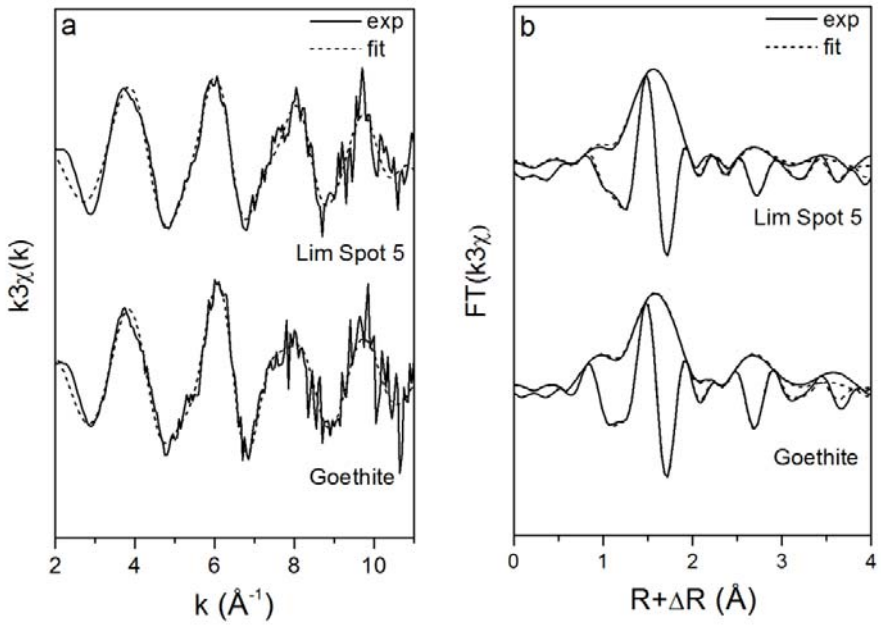

638

639 **Figure 9.** Experimental and fitted Ni K-edge EXAFS spectra (a), and magnitude and

640 imaginary part of their Fourier transforms (b), for limonite Spot 5 and goethite.

641

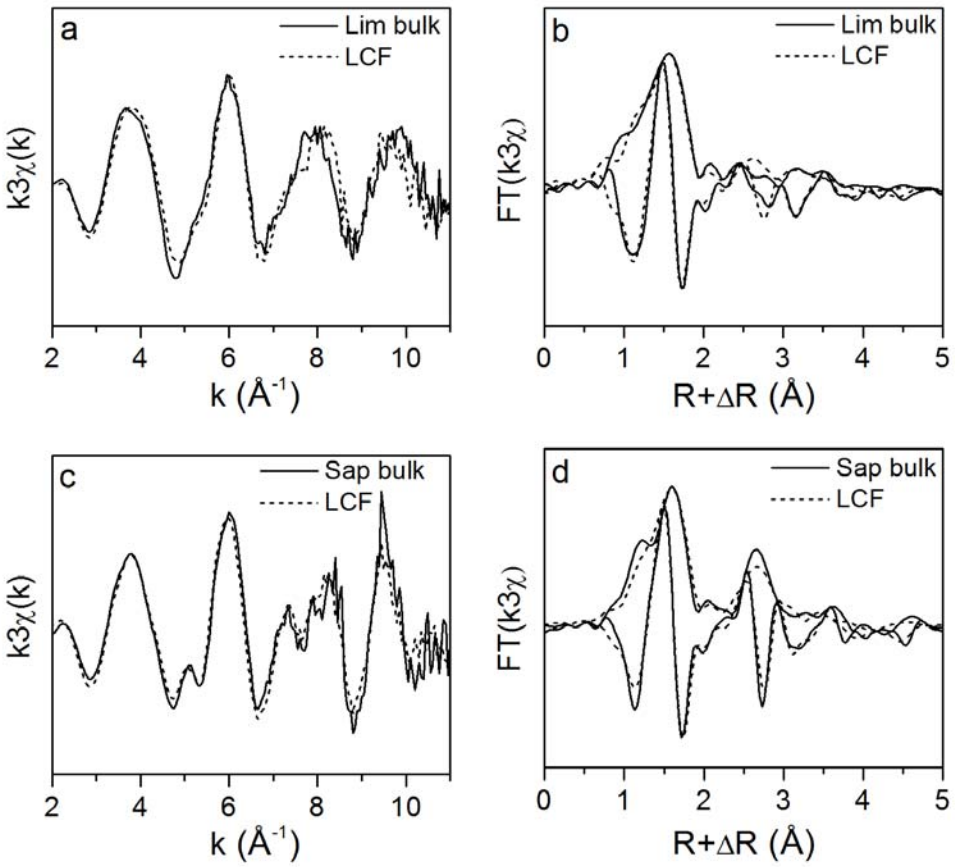

642

643 **Figure 10.** LCF of the EXAFS data (a), and Fourier transform (b), for the bulk
644 limonite as a combination of the spectra derived from goethite, lizardite and lithiophorite; and
645 the EXAFS data (c), and Fourier transform (d), for the bulk saprolite as a combination of the
646 spectra derived from lizardite, asbolane and goethite.

647